Optimization of a fluidic 3D control in a transonic channel flow

Quentin Chanzy, Eric Garnier, Reynald Bur

Association Aéronautique et Astronautique de France

54th 3AF International Conference on Applied Aerodynamics
25 — 27 March 2019, Paris – France

FP69-AERO2019-chanzy

OPTIMIZATION OF A FLUIDIC 3D CONTROL IN A TRANSONIC CHANNEL FLOW.

Quentin Chanzy[(1)], Eric Garnier[(2)] and Reynald Bur[(3)]
[(1)]*ONERA, DAAA AMES, 92190 Meudon, France, qchanzy@onera.fr*
[(2)]*ONERA, DAAA MASH, 92190 Meudon, France, egarnier@onera.fr*
[(3)]*ONERA, DAAA AMES, 92190 Meudon, France, rbur@onera.fr*

ABSTRACT

In this work, flow control of transonic shock wave boundary layer interactions is investigated. A wind-tunnel experiment featuring the Délery bump is considered and RANS simulations are carried out to compute the flow inside the test section. The massive separation due to shock wave boundary layer interaction is controlled by fluidic Vortex Generators(VGs). A two steps Kriging optimization of the pitch and skew angles of twelve VGs is performed. The second step consisting in a precise optimization of the control of the corner flow separation. The goal of these optimizations is to minimize the total pressure losses through the shock wave and along both the boundary layer and the corner flows.

1. INTRODUCTION

Conceiving the air intake remains a preeminent challenge during the design process of a supersonic aircraft. The difficulty lies in the fact that the shock wave necessary to this mechanism is going to interact with the turbulent boundary layer. The well known phenomenon of Shock Wave Boundary Layer interaction(SWBLI) often provokes the separation of the flow. Therefore this separation leads to losses, inhomogeneities and instationarities of the flow. This interaction has been widely studied (see [8, 1, 9, 13] among others), and the instationarities have been linked to the separation bubble. In order to prevent these drawbacks, many control devices have been studied: bleeding, blowing, adaptative geometries like 2D and 3D bumps, diverters, and Vortex Generators(VGs)(see [21, 24] for example). These methods require a full understanding of the complete problem. They should improve the efficiency of the whole air intake, taking into account their added mass and relative energy efficiency. The scope of this physic field is detailed including its fallacies in [6]. In this study, the authors choose to investigate the air jet vortex generators from a full 3D point of view. This control method seems promising as it displays the same advantage as the mechanical VGs which have been proven to be efficient to reduce the separation zone(see [20, 19, 26, 3]) and it has the advantages of being energy efficient and easily turn off when not necessary and so not to be a drawback in other flight configurations.

The always ongoing advances in calculation power allows to set up optimization process which manage to chose the numerous inherent parameters of this type of control. This paper develops a optimization process focusing on the skew and pitch angles of the air VGs and the control of the global flow separation including the effect of the corner flow.

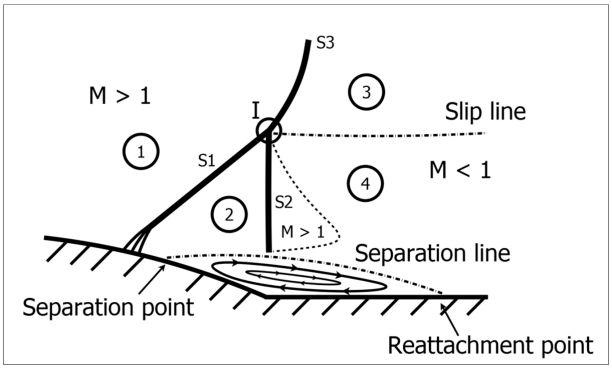

Figure 1: Shock Wave Boundary Layer Interaction (from [23]).

This numerical study is realized on the Délery bump

configuration of the S8Ch wind tunnel of the ONERA Meudon Center which is detailled in [3, 22, 23]. The shape of the bump has been specially designed to induce a strong interaction between the boundary layer and the shock at a nominal Mach number being equal to 1.4, which generates an extended separated zone. A sketch of the interaction is presented in Fig. 1. The stagnation conditions of the flow are near ambient pressure and temperature: $pst = 0.96 \cdot 10^5 \pm 300$ Pa and $Tst = 300 \pm 10$ K. The incoming boundary layer is turbulent and their properties just upstream of the interaction obtained by LDV measurments are: physical thickness $\delta = 3.9$ mm, displacement thickness $\delta_1 = 0.46$ mm, momentum thickness $\theta = 0.25$ mm, and incompressible shape parameter $Hi = 1.6$. The associated unit Reynolds number is around $14 \cdot 10^6$ m^{-1}, which leads to a value of $Re_\theta = 3500$ for the incoming flow.

Firstly, the numerical model used is presented, secondly the optimization process is detailed. It is then applied to the boundary layer separation before a second step of optimization specifically dedicated to the corner flow separation.

2. NUMERICAL MODEL

2.1 Overset Meshes

First of all, in order not to have to mesh again the whole wind tunnel at each vortex generators configuration, we choose to use structured overset meshes. The whole preprocess has been handled using the ONERA software Cassiope [2].

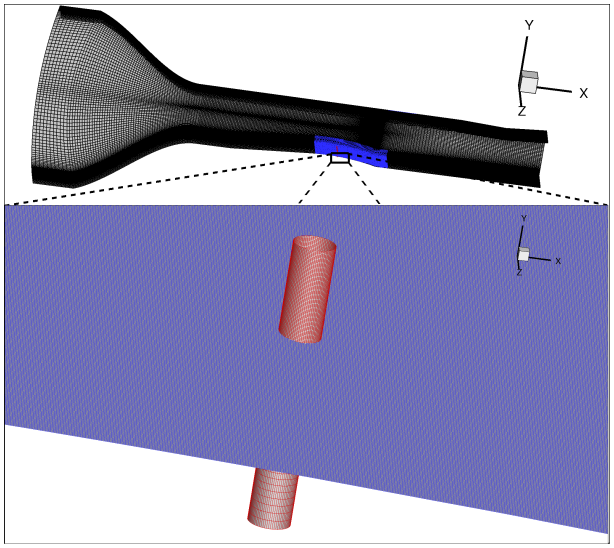

Figure 2: Overset meshes of the wind tunnel with fluidic VGs: fine mesh, jets' meshes and coarser mesh.

The meshes are on display on Fig. 2. The main idea was to have a really fine mesh close to the VGs position

Table 1: Mesh characteristics

	Number of Points
Jet	252 681
Fine mesh	60 839 100
Coarser mesh	4 922 640

in order to fully capture the flow coming from the jets and their interaction with the incoming boundary layer. The principle characteristics of the meshes are summed up in table 1. Close to the walls, the cells are lower than 2 μm which results in a dimensionless wall distance lower than 1 almost everywhere. The boundary layers thicknesses are described using about 50 points. This allows to capture at the same location than the measured one, a boundary layer thickness $\delta = 3.3$ mm, a displacement thickness $\delta_1 = 0.42$ mm and an incompressible shape parameter $H_i = 1.33$ which are close to the one measured experimentally in the wind tunnel by [3].

2.2 Boundary conditions and initial states

In order to accelerate the convergence of the calculations, three initial states have been used. They correspond to different Mach number of the same stagnation conditions $P_{i0} = 0.96 \cdot 10^5$ Pa and $T_{i0} = 300$ K. The first initial state of $Ma = 0.01$ is imposed on the almost static zone in the convergent of the channel, the second state with a $Ma = 0.6$ is imposed on the central part of the test section-including the first throat being the bump- and the last one with $Ma = 1.3$ is used to initialize the second throat which controls the flow rate.

At the entrance of the wind tunnel a subsonic injection condition is imposed using P_{i0} and the stagnation enthalpy corresponding to the first state. At the end of the diffuser, a condition of supersonic outflow is imposed. As the mesh only represents half of the wind tunnel, a condition of symmetry is imposed on the median plane. Everywhere else is imposed a condition of viscous wall.

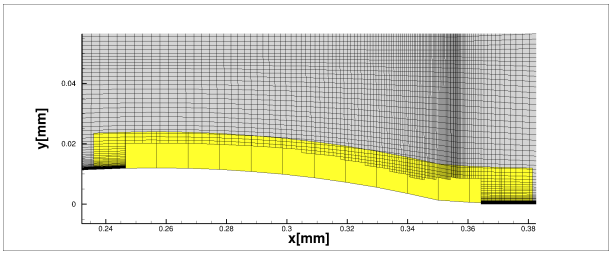

Figure 3: Illustration of the blanking process.

When the jets are added, the coarser mesh is blanked by the fine mesh using a Cassiopee function. The process is illustrated on Fig. 3. At least two cells of each mesh are kept inside of the overset mesh in order to do a proper interpolation. Some other examples of the use of

this function can be found in [16]. Furthermore, the lower wall of the fine mesh is set to a doubly defined condition, meaning that the wall is considered as viscous wall, yet the cells crossed by a jet the wall are considered an overlap boundary.

2.3 Solver

The structured RANS computations are executed with an Onera's in home software: elsA. Informations on this computing code can be found in [4]. This software uses a cell-centered finite volume discretization on structured point-matched and overset grids.The spatial and time integration are respectively carried out using a upwind second-order Roe scheme with Harten entropic correction and a backward-Euler scheme with implicit lower/upper symmetric successive overrelaxation.

The turbulence is modeled using the one-equation SpalartAllmaras (SA) model with the quadratic constitutive relation correction [7]. This correction enriched the Boussinesq relation with anisotropic terms. This allows to improve the precision of the model in the corner flow separation zone.

The calculation are processed on a NEC cluster, more precisely on 256 cores distributed on 10 processors. It takes an equivalent of 3 800h CPU to achieve 30 000 iterations and a proper convergence of the residuals.

2.4 Reference case

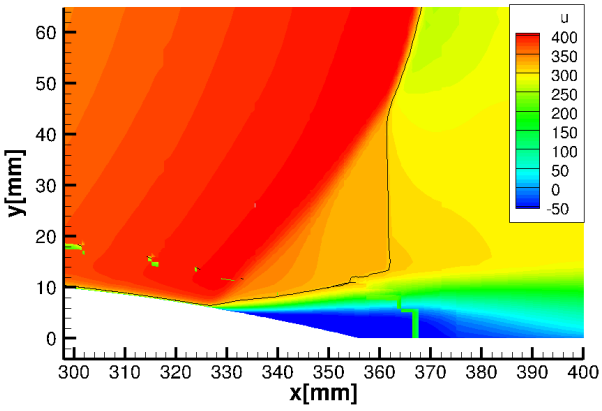

Figure 4: Longitudinal velocity field at the symmetry plane of the wind tunnel calculated using elsA.

The uncontrolled reference case is calculated in order to have a comparison with experimental data. The symmetry plane of the wind tunnel calculated using the process detailed above is compared to 2D PIV results obtained by [22] in Fig.4 and Fig.5. The longitudinal velocity fields are very well matching and the size of the separated zone in the streamwise direction is well predicted even if the height of the bubble is slightly overestimated. Nota bene, the green cells in the red and blue area on Fig.4 are the cells of the fine mesh outside of the interpolation zone and thus do not reflect an error in the computation.

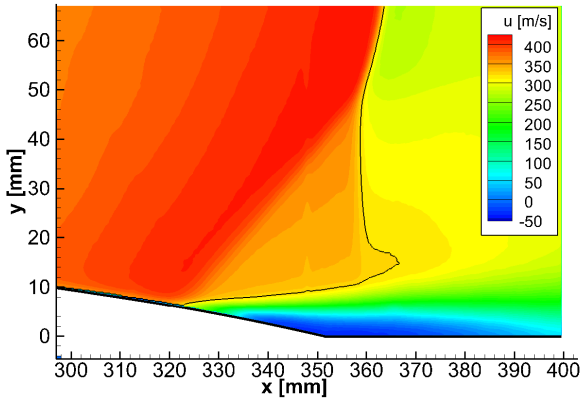

Figure 5: Longitudinal velocity field at the symmetry plane of the wind tunnel measured using 2D PIV method from [22].

3. OPTIMIZATION APPROACH: A KRIGING ALGORITHM

In order to proceed to an optimization of several parameters of the control, an optimization method is set up. The idea is to be able to minimize an objective function described in 4.2 with respect to some parameters described in 4.1 and 5.1. As the phenomena of the interactions between a jet and a cross flow and between a vortex and a shock wave can be really non linear, a kriging algorithm is chosen.This method has been widely employed in various optimization processes, such as for example: porous media [10], aerodynamic design [17], fluid structure interaction [5]. It has the advantage of not inferring the smoothness of the function. Furthermore as the objective function can be really flat with only very localized maxima, this method of search should be quicker than a conventional Newton method. Another method would have consisted in running an adjoint state method to calculate the gradient, nevertheless the size of the mesh prevents us from using this methodology.

The different sequences of the method are described in Algo.1.

Algorithm 1 Kriging optimisation

1: Sampling Plan

- Generation of the 7 initial sampling points with a Latin hypercube sampling method

2: Observations

- Evaluation of these designs with elsA.→Sec. 2

3: Construction of the Surrogate

- Construction of a surrogate model using Kriging method

4: Search of the Infill Criterion

- Construction of the model of the Expected Improvement
- Search of the maximum of the Expected Improvement thanks to a Genetic Algorithm.

5: Addition of a New Design

- Evaluation of the new design at the maximum of the Expected Improvement with elsA.
- Addition of the new design to the model back to step 3.

After evaluating the sampling plan, the method called Kriging is used to construct a first model (see 3 of the algorithm).. This method is explained in [11], [12] and [18]. The main idea when building a model is to use a base of functions with which you calculate the model at each point of the exploration space.

In Kriging, the basis functions are defined in Eq. 1, each i^{th} one linked to a i^{th} sampling point of the n points already measured.

$$\psi^i(x) = \exp(-\sum_{k=1}^{n} \theta_k |x_j^i - x_j|^{p_k}) \quad (1)$$

With x_j^i, x_j the coordinates in the j^{th} dimensions of respectively x^i, x, the i^{th} sampling point and the evaluation point. The θ_k and p_k are variable parameters.

These functions are close to a Gaussian with parameters θ_k and p_k which allow us to balance the influence of each sample point in every dimension in order to find the best model. These functions takes advantages of the fact that you are more certain of the validity of your model near to a sampling point and of the fact that the function can change more or less quickly near to each sampling point. In our case only the θ_k parameters are optimized using a genetic algorithm and the p_k parameters are kept equal to 2.

4. FIRST OPTIMIZATION: THE SEPARATION'S CONTROL

4.1 Optimization parameters

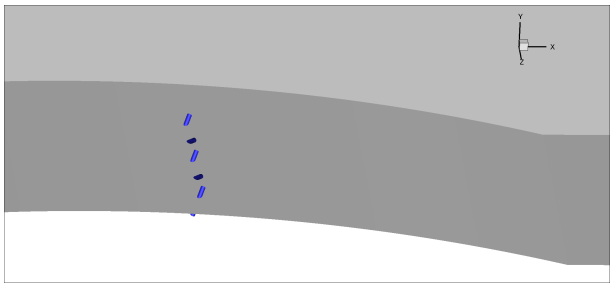

Figure 6: Positions of the jets.

The achievement of the control depends on a wide variety of parameters: the numbers of jets, their lateral and longitudinal positions, their pressure of injection, their pitch and skew angles for each of them. In order to have a reasonable time of calculation, only two parameters are optimized in a first approach. The others parameters are chosen thanks to some first trials and literature results on the mechanical micro vortex generators. The basic configuration is defined as follows: ten VGs are positioned in the spanwise direction of the channel, separated by 2.1 δ (with a bigger gap in the center of the channel due to the presence of a sensor) and 12 δ in front of the shock wave boundary layer interaction which was the best location determined in a previous study with the same interaction [3]. The positions of the jets can be seen on half of the wind tunnel on Fig. 6. The total injection pressure is fixed to 2 bar. The jets diameters are fixed to 1 mm. This is done to ensure a small mass flow rate and a small momentum coefficient c_μ defined in Eq. 2 which are main criteria of efficiency for such fluidic control devices. The momentum coefficient c_μ characterizes the energy of the jets compare to the whole channel.

$$c_\mu = \frac{\Sigma \rho_{jet} U_{jet}^2 S_{jet}}{0.5 \rho_\infty U_\infty^2 S_0} \quad (2)$$

It should be noticed that the real shape of injection is an ellipse which varies with respect to the pitch and skew angles.

Furthermore, the VGs are chosen to be oriented in contra-rotative angles. Previous studies (as [4] for instance) demonstrated that even if the vortices generated by a contra-rotative pair of VGs are more likely to appair and thus to generate a weaker region in the boundary layer, they will sustain each other and thus generate a better mixing. Moreover, in a rectangular channel, only one direction VGs will cause a lateral speed which will deteriorate one corner flow strongly. The two angles of the jets are defined on Fig.7 with respect to the local tangents.

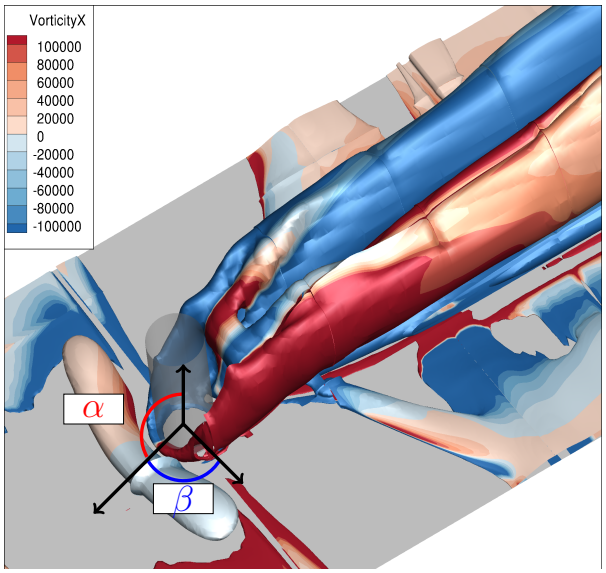

Figure 7: Definition of α and β, respectively pitch and skew angles in the case of the perpendicular jet producing the well known contra-rotative pair of vortices visualized on a Q criterion equal to $3 \cdot 10^8$ isosurface colorized with longitudinal vorticity.

Due to physical constraints, the α angle is only varied between 30°and 150°. The angle β is varied between 0°and 180°. Combined with the pitch rotation, this variation allows to consider all the physical configuration including the reversed jets which are less tested in the literature.

4.2 Objective function: DC50 coefficient

The goal of this study is to reduce the separation zone which should improve both the homogeneity and the total internal energy of the flow after the shock wave boundary layer interaction. In order to quantify the improvement on both of these quantities, a one dimension function has been selected. A criterion, called DC50, is defined based on an existing criterion used by aircraft manufacturers: the DC60 criterion [15, 14]. This criterion is calculated on a slice perpendicular to the channel placed behind the interaction and the separation zone as it can be seen on Fig. 8. It consists of a comparison between the mean stagnation pressure Pi_{mean} in the slice with the worse mean stagnation pressure in a fiftieth of the slice Pi_{zone}. This quantity is divided by the mean kinetic velocity q_{mean} in the slice in order to give an information not only on the homogeneity of the flow but on the conservation of the energy. This criterion is summed up in Eq. 3. The fifty portions of the slice of the reference case(without control) are presented on Fig. 9. The loss of stagnation pressure due to the boundary layer and corner flow separation are clearly visible. The DC50 of the reference case is equal to 0.88. The objective of the optimization will be to minimize this criterion.

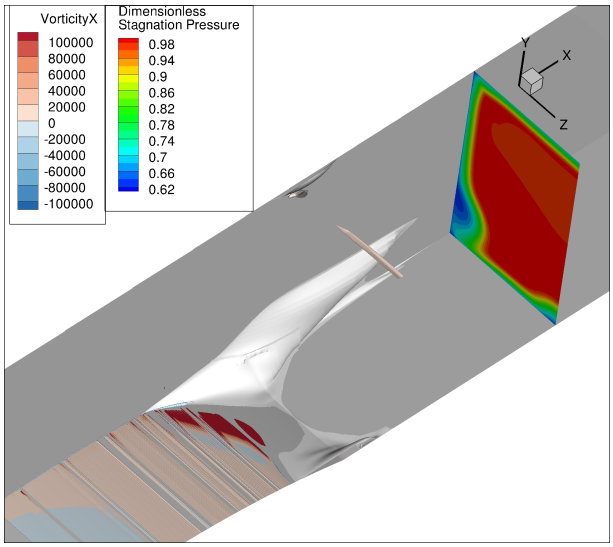

Figure 8: Stagnation pressure non dimensionalized using $P_{i0} = 0.96 \cdot 10^5$ Pa on the DC50 plane at $x = 468$ mm, volume of the reverse flow-white surface- and Q criterion equal to $3 \cdot 10^8$ isosurface colorized with longitudinal vorticity for the reference case.

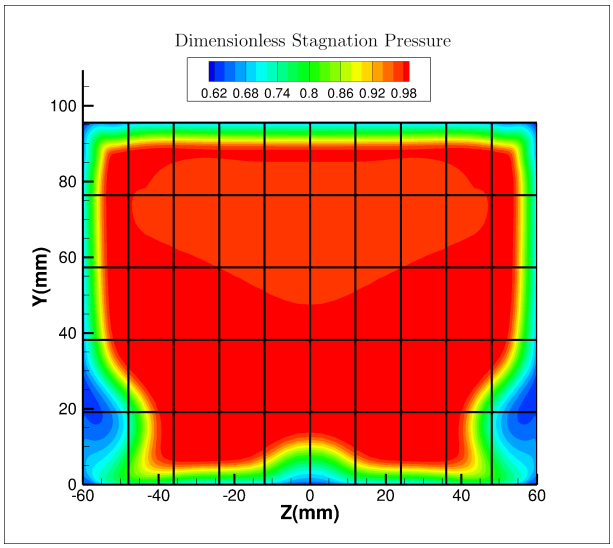

Figure 9: Stagnation pressure non dimensionalized using $P_{i0} = 0.96 \cdot 10^5$ Pa on the transverse plane of the reference case used for the DC50 criterion with the 50 zones.

$$DC50 = \frac{Pi_{mean} - min(Pi_{zone})}{q_{mean}} \quad (3)$$

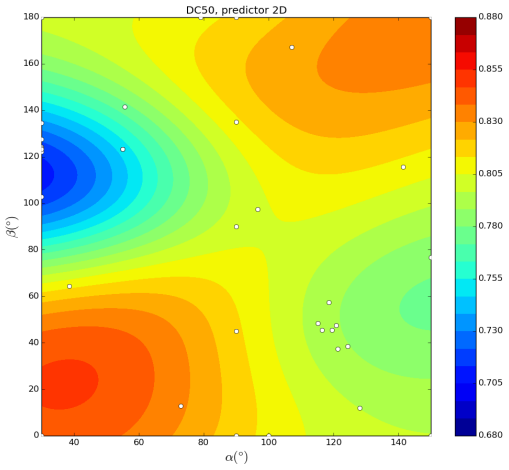

Figure 10: Regression kriging model of the DC50 function with respect to the skew and pitch angles of ten VGs.The white dots represent the calculated cases.

4.3 Results

4.3.1 DC50 model

After 36 iterations of the algorithm, the model does not seem to vary a lot and two main zones of interest appear. Due to the closeness of some calculation points and to the uncertainty of the RANS numerical calculation of the DC50, a regression kriging is used instead of the classical kriging. It allows the model to take into account a small margin of uncertainty and not to try to perfectly fit the calculated points. The model is then improved with four points at no additional numerical cost as they all correspond to the same configuration, indeed, when the pitch angle is fixed to 90 °the skew angle does not have a real signification as the jets remain vertical with respect to the local tangents.

The model is presented on Fig. 10. First of all the upper and lower limits seems to be the same but reversed which is a fair result as when β goes from 0°to 180°the jets are just directed in the opposite direction so α is equal to its complementary angle to 180°. Then the model present a "quasi-central symmetry". This is coherent with the fact that the intensity and position of the vortices generated by the jets symmetric with respect to the centers of the model are symmetric along the longitudinal plane. The difference of level of DC50 is due to the fact that the jets close to the center and the corner of the channel interact differently. The two main zones of interest in blue and green are on the reverse jets zones presented which differs from the previous studies which consider that the preferential angles were $\alpha = 30°$and β =60°.

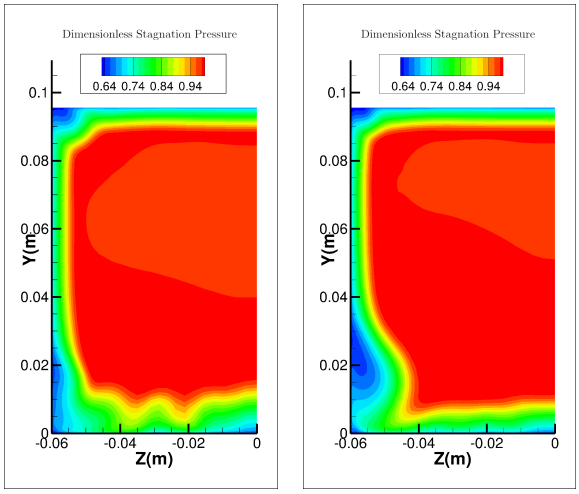

(a) Optimum-Case 28 (b) Sub optimum-Case 12

Figure 11: Stagnation pressure non dimensionalized using $P_{i0} = 0.96 \cdot 10^5$ Pa on the transverse DC50 plane of the best controlled cases of the first optimization.

The best controlled case -Case 28- is for $\alpha = 30°$ and β =102.8°values of angle, the objective function is equal to 0.68 which is already an improvement of 20%. It generates the DC50 slice presented on Fig. 11a and the reverse flow visible on Fig. 12. This configuration is composed of reversed jets with the lateral one pointing outward at the wall. The external jet manages to reduce the impact of the corner flow by inducing a reverse flow upstream and farther from the lateral wall. The corner flow presents a completely different shape and seems to be more efficiently dissipated.

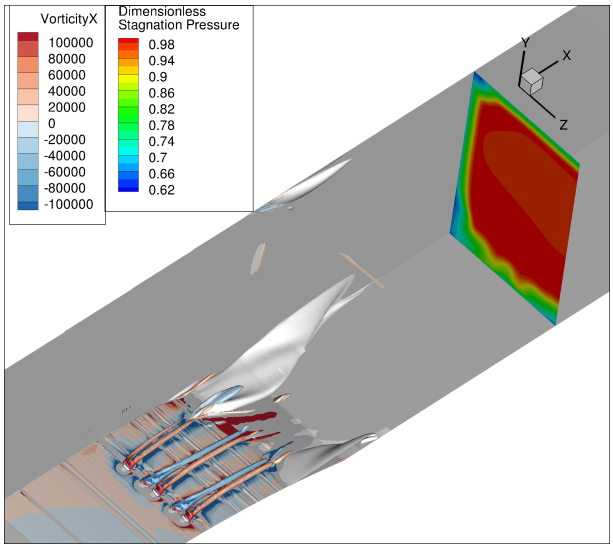

Figure 12: Stagnation pressure non dimensionalized using $P_{i0} = 0.96 \cdot 10^5$ Pa on the DC50 plane at $x = 468$ mm, volume of the reverse flow-white surface- and Q criterion equal to $3 \cdot 10^8$ isosurface colorized with longitudinal vorticity for the optimum-Case 28.

4.3.2 Furthers analysis

The mechanism which makes the optimum control can be explained as follows: this couple angles generates for each jet a pair of same sign longitudinal vorticity as it can be seen on Fig. 13a. This pair of vortices is going to generate a lateral velocity for each pair of vortices. Looking at the development of the vortices farther downstream on Fig. 13b, in the case of the central jets, the two vortices are going to merge when they meet the adjacent opposite vortices and form a new pair of opposite vortices that are going to sustain each other in the downstream flow direction. For the lateral jet, the pair of vortices is going to move closer to the wall and provoked a mixing which induces a weaker boundary layer between the two vortices. This weaker zone is more sensitive to the adverse pressure gradient due to the shock and separates earlier.

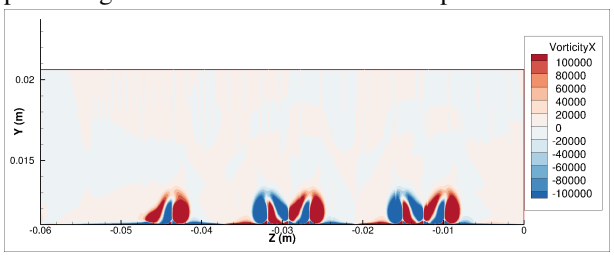

(a) Longitudinale vorticity at x=285mm-Case 28.

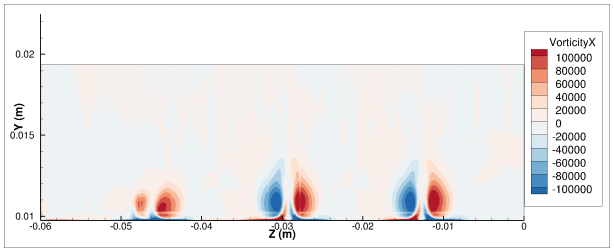

(b) Longitudinal vorticity at x=300mm-Case 28.

Figure 13: Longitudinal vorticity on two transverse planes along the flow.

The conclusion of this first optimization is that the algorithm manage to find an optimum which reduces the value of the objective function and this configuration is composed of slightly reversed jets. Nevertheless, this study emphasizes the fact that the most impacting part of the reverse flow on the DC50 criterion is the corner flow, this has already been highlighted in [25, 27]. To improve the control, a second optimization is considered with a specific jet controlling the corner flow. In order not to allow the central reverse flow to grow while the corner separation diminish, a central control will be conserved. The case chosen for this is the sub optimum case -Case12- with $\alpha = 120°$ and $\beta = 45°$, presented on Fig. 11b and Fig. 14. It generates a DC50 of 0.78 which is only a 10% of improvement however, it controls better the separation and as the lateral jet is going outward the wall, it allows the corner control jet not to interact with the central ones.

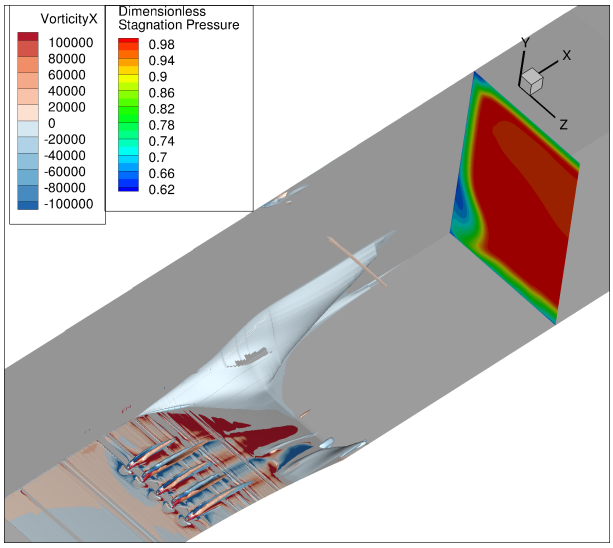

Figure 14: Stagnation pressure non dimensionalized using $P_{i0} = 0.96 \cdot 10^5$ Pa on the DC50 plane at $x = 468$ mm, volume of the reverse flow-white surface- and Q criterion equal to $3 \cdot 10^8$ isosurface colorized with longitudinal vorticity for the sub-optimum-Case 12.

Table 2: Parameters of the second optimization.

Parameter	Min	Max
X position(mm)	260	320
Z position(mm)	38	57.5
Pitch angle $\alpha(°)$	30	150
Skew angle $\beta(°)$	0	180

5. SECOND OPTIMIZATION: THE CORNER FLOW SEPARATION'S CONTROL

5.1 New optimization's parameters

As explained in 4.3.2, the second optimization considers a control with 12 jets, the 10 central ones of the Case 12- $\alpha = 120°$ and $\beta = 45°$, and a jet in each corner to control specifically the corner separation. The positions and orientation of the central jets can be seen on Fig. 15. The optimization will take into account two others parameters for the jet. The longitudinal and lateral position of the jet will be optimized too. The pitch and skew angle will also be optimized. All the parameters' range of variation are summarized in Tab. 2.

The objective function is calculated as in the previous optimization.

The first latine hypercube is of dimension four and thus the initial number of samples is increased to 15. Then the processus of improvement is kept as before except that in order to accelerate the convergence, the new points are calculated 3 by 3. To chose these three points, the

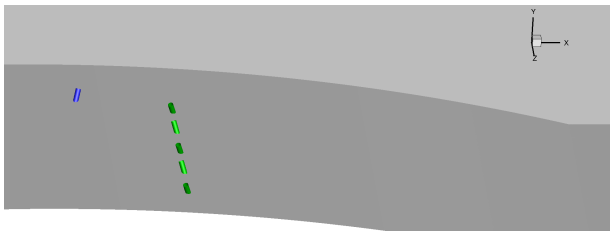

Figure 15: Positions and orientation of the central jets-in green- and a position of the corner jet-in blue.

model is updated with the first optimum of the expected improvement predicted value and a new model is tuned before a new research of the maximum of the expected improvement. The same technique is used for the third point. Once the three points have been calculated, their real value are added to the model of the previous step before it is tuned again.

The algorithm enriched the model up to 122 points. It converged to a zone of interest.

5.2 Results

The model calculated is almost constant with a value close to the DC50 of the Case 12 meaning that the corner jet does not improve the control at these positions. Nonetheless, the algorithm managed to find a zone of interest which is presented on a 2 dimension map with α and β fixed respectively to 30°and 106°on Fig. 16.

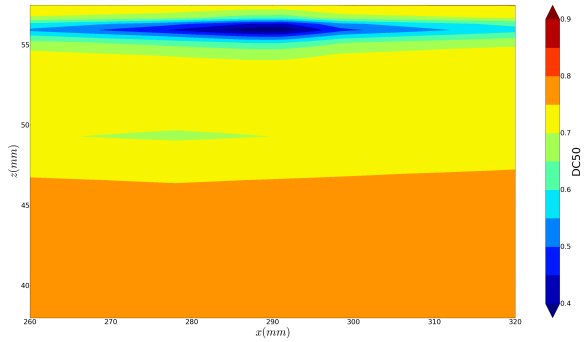

Figure 16: Zone of interest of the second DC50 model.

In this small zone close to the wall, the jets manage an important improvement of the DC50. The longitudinal position seems to be less sensitive than the lateral one inducing that the control efficiency resides in the position of the vortex with respect to the sidewall much more than to its intensity.

The best controlled case found is $\alpha = 30°$ and $\beta = 106.0°$, the objective function is of 0.34 which leads to an improvement of 60% of the DC50. It generates the DC50 slice presented on Fig. 17 and the reverse flow visible on Fig. 18.

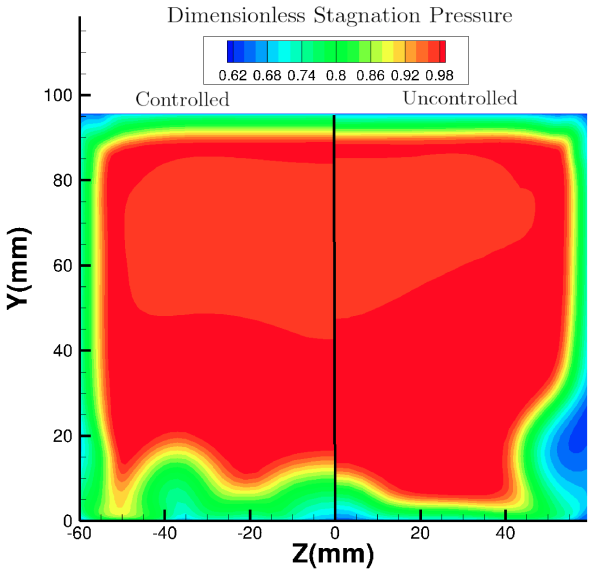

Figure 17: Stagnation pressure non dimensionalized using $P_{i0} = 0.96 \cdot 10^5$ Pa on the transverse DC50 plane of the best controlled case of the second optimization-left- and uncontrolled-right-.

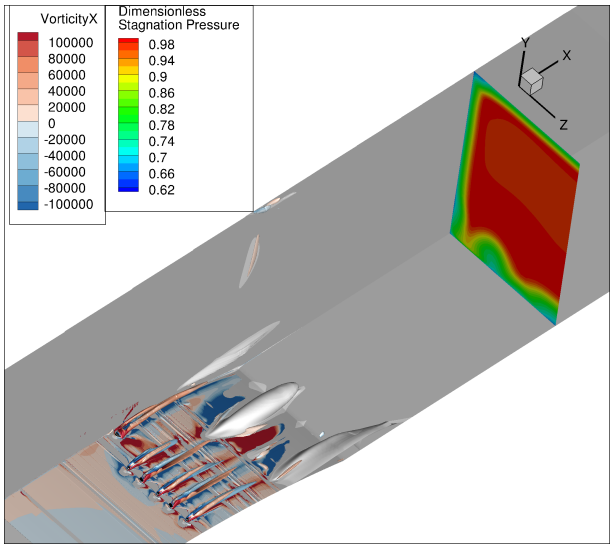

Figure 18: Stagnation pressure non dimensionalized using $P_{i0} = 0.96 \cdot 10^5$ Pa on the DC50 plane at $x = 468$ mm, volume of the reverse flow-white surface- and Q criterion equal to $3 \cdot 10^8$ isosurface colorized with longitudinal vorticity for the optimum.

The corner flow separation is not anymore present and is replaced by two smaller separation zones along each side of the corner. These separation zones have smaller impact on the total pressure downstream. The mechanism of the corner flow vortex is presented on Fig. 19 and its impact on the longitidinal momentum is compared to the uncontrolled case on the Fig. 20 and Fig. 21 respec-

tively. By being able to stuck to the corner, the vortex manages to reinject energy into the boundary layer of the corner flow and thus to prevent the separation. This result is closed to the results found experimentally in [27] and confirm the interest of controlling both the boundary layer and the corner separation as a global phenomenon as done in [25].

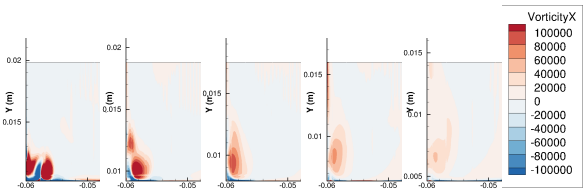

Figure 19: Longitudinal vorticity on five transverse planes close to the corner, along the flow at x equal 295, 305, 315, 325 and 335mm from left to right for the optimum case of the second optimization.

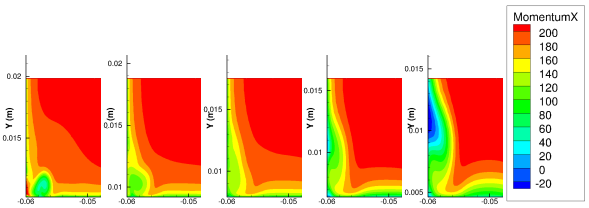

Figure 20: Longitudinal momentum on five transverse planes close to the corner, along the flow at x equal 295, 305, 315, 325 and 335mm from left to right for the optimum case of the second optimization.

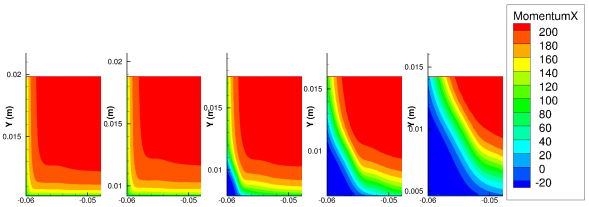

Figure 21: Longitudinal momentum on five transverse planes close to the corner, along the flow at x equal 295, 305, 315, 325 and 335mm from left to right for the uncontrolled case.

6. CONCLUSION

The optimization process presented in this study turns out to be an effective process which managed to find an efficient air vortex generator control of the case studied. It highlighted the interest of having reversed jets to control the flow destabilized by the strong interaction, this configuration giving some other structure and so other induced velocity to the vortices generated. This fluidic flow control configuration with reversed jets has not been studied yet at the authors knowledge. The control configuration is really efficient as it reduces the DC50 criterion of 60% with a momentum coefficient c_μ of only 0.03%.

Following this numerical study, an experimental test of the best controlled configuration is actually being tested in the wind tunnel in order to deeply understand the mechanism of control and to characterize its unsteady features.

7. AKNOWLEDGMENT

This work was carried out with a grant of the Direction Générale de l'Armement. Their support is gratefully acknowledged.

REFERENCES

[1] Holger Babinsky and John K. Harvey. *Shock Wave-Boundary-Layer Interactions*. Cambridge University Press, September 2011.

[2] Christophe Benoit, Stéphanie Péron, and Sâm Landier. Cassiopee: A CFD pre- and post-processing tool. *Aerospace Science and Technology*, 45:272–283, Sep 2015.

[3] Reynald Bur, Didier Coponet, and Yves Carpels. Separation control by vortex generator devices in a transonic channel flow. *Shock Waves*, 19(6):521–530, 2009.

[4] Laurent Cambier, Sébastien Heib, and Sylvie Plot. The Onera elsA CFD software: input from. *Mechanics & Industry*, 14(3):159–174, 2013.

[5] Q. Chanzy and A. J. Keane. Analysis and experimental validation of morphing UAV wings. *The Aeronautical Journal*, 122(1249):390–408, March 2018.

[6] WJ Crowther, M Jabbal, and SC Liddle. Flow control fallacies: a review of commonpitfalls in flow control research. *Proceedings of the Institution of Mechanical Engineers, Part G: Journal of Aerospace Engineering*, 225(1):1–11, 2011.

[7] Julien Dandois, Vincent Brunet, Pascal Molton, Jean-Charles Abart, and Arnaud Lepage. Buffet control by means of mechanical and fluidic vortex generators. In *5th Flow Control Conference*, 2010.

[8] Jean M. Delery. Shock wave/turbulent boundary layer interaction and its control. *Progress in Aerospace Sciences*, 22(4):209–280, January 1985.

[9] David S Dolling. Fifty years of shock-wave/boundary-layer interaction research: what next? *AIAA journal*, 39(8):1517–1531, 2001.

[10] A. J. Evans, C. P. Caulfield, and Andrew W. Woods. Linear estimation of flux sensitivity to uncertainty in porous media. *Journal of Fluid Mechanics*, 768:600–622, Apr 2015.

[11] Alexander Forrester, Andras Sobester, and Andy Keane. *Engineering design via surrogate modelling: a practical guide*. John Wiley & Sons, 2008.

[12] Alexander IJ Forrester and Andy J Keane. Recent advances in surrogate-based optimization. *Progress in Aerospace Sciences*, 45(1):50–79, 2009.

[13] Datta V. Gaitonde. Progress in shock wave/boundary layer interactions. *Progress in Aerospace Sciences*, 72:80 – 99, 2015.

[14] E. Garnier. Flow Control by Pulsed Jet in a Curved S-Duct: A Spectral Analysis. *AIAA Journal*, 53(10):2813–2827, 2015.

[15] Eustace Laurence Goldsmith and John Seddon. *Practical intake aerodynamic design*. Amer Inst of Aeronautics &, 1993.

[16] David Hue, Quentin Chanzy, and Sâm Landier. DPW-6: Drag Analyses and Increments Using Different Geometries of the Common Research Model Airliner. *Journal of Aircraft*, Jan 2017.

[17] DJ J. Toal, Neil W Bressloff, and Andy J Keane. Kriging hyperparameter tuning strategies. *AIAA journal*, 46(5):1240–1252, 2008.

[18] Donald R Jones. A taxonomy of global optimization methods based on response surfaces. *Journal of global optimization*, 21(4):345–383, 2001.

[19] S. Lee, E. Loth, and H. Babinsky. Normal shock boundary layer control with various vortex generator geometries. *Computers & Fluids*, 49(1):233 – 246, 2011.

[20] John C Lin. Review of research on low-profile vortex generators to control boundary-layer separation. *Progress in Aerospace Sciences*, 38(45):389–420, May 2002.

[21] J.-P. Rosenblum. An overview of flow control activities at Dassault Aviation over the last 25 years. *The Aeronautical Journal*, 120(1225):391–414, March 2016.

[22] Fulvio Sartor, Gilles Losfeld, and Reynald Bur. PIV study on a shock-induced separation in a transonic flow. *Experiments in fluids*, 53(3):815–827, 2012.

[23] Fulvio Sartor, Clément Mettot, Reynald Bur, and Denis Sipp. Unsteadiness in transonic shock-wave/boundary-layer interactions: experimental investigation and global stability analysis. *Journal of Fluid Mechanics*, 781:550–577, 2015.

[24] F Ternoy, J Dandois, F David, and M Pruvost. Overview of onera actuators for active flow control. *HAL archives-ouvertes.fr*, pages 1–14, August 2015.

[25] Neil Titchener and Holger Babinsky. Shock Wave/Boundary-Layer Interaction Control Using a Combination of Vortex Generators and Bleed. *AIAA Journal*, 51(5):1221–1233, 2013.

[26] Neil Titchener and Holger Babinsky. A review of the use of vortex generators for mitigating shock-induced separation. *Shock Waves*, 25(5):473–494, 2015.

[27] Xue Xiang and Holger Babinsky. An experimental study of corner flow control applied to an oblique shock-wave/boundary-layer interaction. In *2018 AIAA Aerospace Sciences Meeting*, 2018.